Acta Crystallographica Section D
Biological Crystallography
ISSN 0907-4449

Structure of mouse L-chain ferritin at 1.6 Å resolution

Thierry Granier,[a]* Bernard Gallois,[a] Béatrice Langlois d'Estaintot,[a] Alain Dautant,[a] Jean-Marc Chevalier,[a] Jean-Marc Mellado,[a] Carole Beaumont,[b] Paolo Santambrogio,[c] Paolo Arosio[c] and Gilles Precigoux[a]

[a]Unité de Biophysique Structurale, UMR CNRS 5471, Université Bordeaux I, Bâtiment B8, Avenue des Facultés, 33405 Talence CEDEX, France, [b]INSERM U409, Faculté de Médecine Xavier Bichat, 16 Rue Henri Huchard, 75870 Paris CEDEX 18, France, and [c]Unit of Protein Engineering, Dibit, San Raffaele Scientific Institute, Via Olgettina 58, 20132 Milano, Italy

Correspondence e-mail: t.granier@ubs.u-bordeaux.fr

Cubic *F*432 crystals of recombinant mouse L-chain apoferritin were obtained by the hanging-drop technique with ammonium sulfate and cadmium sulfate as precipitants. The structure was refined to 2.1 and 1.6 Å resolution from data obtained at room temperature and under cryogenic conditions, respectively. The structure of an eight-amino-acid loop insertion in the mouse sequence is found to be highly disordered both at room temperature and at low temperature.

Received 26 February 2001
Accepted 30 May 2001

PDB Reference: mouse L-chain ferritin, 1h96.

1. Introduction

Ferritin, the ubiquitous iron-storage protein, has been largely investigated, but unravelling the different features of the structure–function relationships in this protein is still a matter of concern (for reviews, see Harrison & Arosio, 1996; Harrison *et al.*, 1998; Chasteen & Harrison, 1999). Its three-dimensional multimeric structure, which was determined 20 y ago (Clegg *et al.*, 1980), and its heteropolymeric composition in vertebrates (Adelman *et al.*, 1975) as well as the multiple active sites (iron entry-route channels, ferroxidase centre, mineral nucleation site) are some of the major factors which account for the complexity of its function.

Ferritins are multimeric proteins consisting of 24 subunits. Each of them (15–20 kDa) consists of a four (a, b, c, d) α-helix bundle to which a fifth small α-helix e is attached at the C-terminal end. The 24 subunits assemble in a 432 point symmetry. The multimer has a spherical shape (diameter 120–130 Å), with an inner cavity of about 80 Å diameter; this cavity can host up to 4500 iron ions stored as hydrous ferric oxide. Natural ferritins isolated from vertebrates are heteropolymers made of various types of subunits, named H, L or M, with different sequences, whereas bacterial and plant ferritins have been shown to be mainly homopolymers of H-type chains, the subunit associated with a ferroxidase activity.

Several structures of ferritin have been refined to a resolution of 2.0 Å or better: recombinant bullfrog L-chain ferritin (rBfLF; Trikha *et al.*, 1995; PDB code 1rcd), recombinant horse L-chain ferritin (rHoLF; Gallois *et al.*, 1997; PDB code 1dat; Hempstead *et al.*, 1997; PDB code 1aew), variant human H-chain ferritin (rHuHF; Hempstead *et al.*, 1997; PDB code 2fha), the best resolution (1.85 Å) being reached for the variant bullfrog H-chain ferritin (rBfHF; Takagi *et al.*, 1998; PDB code 1bg7).

In the course of our structural investigation on recombinant mouse L-chain ferritin (rMoLF; Granier *et al.*, 2000), we obtained three crystal forms obtained from different crystallization conditions: a first set of crystals (tetragonal and monoclinic forms) was obtained from solutions which did not contain any metal-ion salt and diffracted to a resolution of

Table 1
Data-collection statistics.

Values in parentheses correspond to the last resolution shell.

Temperature (K)	300	100
Crystal dimensions (mm)	0.35 × 0.33 × 0.15	0.62 × 0.60 × 0.15
Crystal-to-film distance (mm)	159	95
Oscillation range φ (°)	24.0	22.5
$\Delta\varphi$ (°) rotation per frame	1.5	0.9
Exposure time per frame (s)	900	4800
Unit-cell parameters (Å)	182.5	180.82
Resolution range (Å)	20–2.10	20–1.60
Last shell (Å)	2.21–2.10	1.64–1.60
$N_{\rm measured}$	83602 (10310)	158991 (8894)
$N_{\rm unique}$	15681 (2030)	32292 (2042)
Completeness (%)	98.5 (91.3)	95.7 (83.8)
Multiplicity	5.6 (5.3)	4.9 (4.4)
$R_{\rm meas}$†	0.141 (0.48)	0.079 (0.43)
$R_{\rm sym}$†	0.126 (0.40)	0.071 (0.38)
PCV†	0.150 (0.56)	0.094 (0.56)
$\langle I/\sigma(I)\rangle$	6.0 (1.9)	9.3 (1.9)
$[I > 3\sigma(I)]$ (%)	87 (75)	79 (54)

† See Diederichs & Karplus (1997) for definitions.

Table 2
Refinement parameters.

Values in parentheses correspond to the last resolution shell.

Temperature (K)	300	100
Resolution shell (Å)	20.0–2.10	19.0–1.60
Last shell (Å)	2.21–2.10	1.64–1.60
$R_{\rm fac}$	0.16 (0.15)	0.16 (0.22)
$R_{\rm free}$	0.20 (016)	0.19 (0.27)
DPI† (Å)	0.143	0.071
EME‡ (Å)	0.07	0.05
R.m.s. deviations		
Bonds (Å)	0.009	0.009
Angle distances (Å)	0.023	0.022
Planar 1–4 distances (Å)	0.027	0.027

	300 K		100 K	
Protein atoms	No.	$\langle B\rangle$ (r.m.s.) (Å^2)	No.	$\langle B\rangle$ (r.m.s.) (Å^2)
Main chain	672	13.6 (4.5)	677	8.41 (2.9)
Side chain	653	17.6 (7.3)	694	11.5 (6.1)
Water molecules				
First shell	124	33.0 (12.8)	192	22.9 (10.8)
Second shell	27	40.6 (8.5)	74	32.0 (11.7)
Third shell	—	—	20	38.6 (8.8)
Cd^{2+} ions	4	32.8 (10.3)	9	20.8 (5.8)

† Diffraction-component precision index as defined by Cruickshank (1999). ‡ Expected maximal error. See definition in Vaguine *et al.* (1999).

2.46 Å. Using cadmium sulfate as the crystallization agent, we obtained crystals of the cubic *F*432 form isomorphous to rHoLF, variant rHuHF, rBfLF and rBfHF crystals. Cubic crystals of rMoLF diffract to 2.1 Å at room temperature. Under cryogenic conditions and using Cu *Kα* X-ray radiation generated by a rotating anode, we collected data to a resolution of 1.6 Å. Among the reasons which led us to investigate the structure of rMoLF, one of them concerns the specific mouse L-chain sequence: it exhibits, along with rat L-chain ferritin sequence, an eight-amino-acid insertion PAQTGAPQ in the exposed loop connecting helices *d* and *e*. In a previous study of recombinant rat L-chain ferritin crystals (Lawson, 1990), this insertion was found to be highly disordered. We present here the structure of the cubic form of rMoLF refined to a resolution of 1.6 Å. We briefly compare it with the room-temperature structure refined to 2.1 Å resolution: in both cases, the *de* loop insertion is highly disordered. Nevertheless, the low-temperature structure allowed us to improve the model: a few more partially occupied cadmium-binding sites and their coordination shell pattern were determined, several additional side chains were positioned and the ordered water shell was notably built up. Differences from rHoLF and rBfLF are also briefly described.

2. Crystallization and data collection

Expression and purification have been described previously (Santambrogio *et al.*, 2000). An Ala residue replaces the reported Thr at position 121 (Beaumont *et al.*, 1989), a substitution arising from a G→A transition possibly caused by a PCR error. The substitution did not affect protein assembly, stability or ferritin iron-uptake functionality (not shown). The subunit molecular weight is 20 641 Da (182 amino acids). Crystallization was performed using the hanging-drop vapour-diffusion method in Linbro plates. The best crystals were obtained in a few days at 293 K in hanging drops produced by mixing 3 µl of protein solution at a concentration of 3.5 mg ml^{-1} in 20 m*M* Tris pH 7.4 and 3 µl of precipitant solution composed of 0.92 *M* ammonium sulfate, 0.4% $CdSO_4$ and 3 m*M* NaN_3. Drops were equilibrated against 1 ml of the same precipitant solution. Crystals had approximate dimensions of 0.5 × 0.5 × 0.15 mm. X-ray diffraction experiments were conducted using an X-ray source (graphite monochromated Cu *Kα*, λ = 1.5418 Å) provided by an Enraf–Nonius FR571 rotating-anode generator operating at 40 kV and 50 mA. Diffraction data were collected on a 300 mm MAR Research image-plate scanner, processed with the program *MOSFLM* (Leslie *et al.*, 1986) and further scaled with the program *SCALA* (Collaborative Computational Project, Number 4, 1994). The data statistics are gathered in Table 1. Low-temperature data were obtained by the flash-freezing technique. 30% glycerol was added to the mother liquor. Low temperature (100 K) was obtained by cold nitrogen-gas flow using the Cryostream cooler (Oxford Cryosystems, England). Crystals were mounted on a modified Huber goniometer head equipped with a removable arc (Litt *et al.*, 1998).

3. Refinement

The room-temperature and low-temperature structures were refined using the program *REFMAC* (Murshudov *et al.*, 1997). The starting model was that of rHoLF (Gallois *et al.*, 1997; atomic coordinates from PDB file 1dat). Models were visualized and modified based on $2F_o - F_c$ and $F_o - F_c$ electron-density maps using the graphics programs *TURBO-FRODO* (Roussel *et al.*, 1990) and *XtalView* (McRee, 1993). Water molecules were positioned in well defined $F_o - F_c$ residual

Table 3
Intrasubunit and intersubunit hydrogen bonds and salt bridges observed in rMoLF and rHoLF.

Side chain–main chain		Main chain–side chain		Side chain–side chain	
Donor	Acceptor	Donor	Acceptor	Donor	Acceptor
Hydrogen bonds and salt bridges within a subunit					
Arg5†	Tyr8	Ile4	Ser2	Tyr8†	Gln69
Arg72†	Gln6	Val12†	Ser9	Gln69	Asn17
Asn7†	Ala121	Arg75†	Glu13	Tyr30†	Glu103
Gln69†	Glu13	Gly46†	Glu175	Trp89†	Ser32
Asn17	Arg75	Lys91†	Glu94	Arg72	His124
His23	Leu19	Thr92†	Glu171	Thr92†	Glu171
Asn21	Asp80	Leu125†	Asp122	Gln93	Glu97
Thr29†	Arg25	Glu171	Ser168	Gln108†	Asp112
Ser27†	Ala55			Lys142	Asn146
Tyr133	Gly61			Arg153†	Asn150
Gln86†	Glu88				
Ser118†	His114			Thr91‡	Asp94
Cys126†	Asp122			His114‡	Glu130
Ser131†	Asp127				
Lys136	His132				
Thr149†	Gly145				
Asn150†	Asn146				
Cys48‡	Gly34				
Tyr36‡	Gly90				
Arg75‡	Gly74				
Ser105‡	Val101				
Ser157‡	Arg153				
Salt bridges					
Arg5†	Glu13				
Arg120	Glu11				
Arg39†	Asp41				
Arg39	Glu88				
Lys58†	Glu103				
Lys58†	Glu137				
Arg72†	Asp122				
Arg152	Glu97				
Arg176†	Glu175				
Lys142‡	Asp146				
Hydrogen bonds and salt bridges within a dimer					
Tyr28†	Glu79	Lys83†	Asp80	Ser2†	Asp40
Asn70†	Phe35			Gln3†	Asp40
				Asn70‡	Asp38
Val81†§	Val81§				
Salt bridges within a dimer					
Arg75	Asp40				
Lys67	Asp38				
Hydrogen bonds within a trimer					
Lys104†	Gln3			Asn107†	Gln6
Lys104	Arg5			Arg152	Gln3
Gln6†	Lys104			His124	Asp135
Gln3†	Gly145				
Salt bridges within a trimer					
Lys139	Asp71				
Hydrogen bonds within a tetramer					
Arg176†	Leu177			Tyr172†	Thr178
Lys142†	Asp38				
Thr149†	Asp40				
Arg153†	Val42				
Asn150†	Ala43				
Arg168‡	Leu169	Leu161‡	Ser157		

† Interactions in common with rHoLF. ‡ Interactions observed in rHoLF and not in rMoLF. § Main chain–main chain.

densities with a lower cutoff of 3σ. Cadmium ions were positioned according to anomalous Fourier difference maps with a lower cutoff of 4σ. Refinement characteristics are gathered in Table 2.

3.1. Model quality

$2F_o - F_c$ maps contoured at 1σ have continuous electron density along the subunit backbone, with the exception of the first N-terminus residue, Thr1, the 156–167 segment which corresponds to the *de* loop insertion and the two last C-terminal residues, *i.e.* His181 and Asp182. Of the remaining residues, several side chains could not be positioned, *i.e.* those of Glu11, Arg18, Arg25, Glu45, Glu53, Glu56, Lys91 and Arg120 for the room-temperature structure, and Arg25 and Lys91 for the low-temperature structure. Using the program *SFCHECK* (Vaguine *et al.*, 1999), the lowest density correlation coefficients (D_{corr} = 0.85–0.88) are obtained for the side chains of residues Asp38, Glu60, Glu67 and Gln79 for the room-temperature structure, and the side-chain atoms of residue Glu53 for the low-temperature structure. A Ramachandran plot (Ramachandran *et al.*, 1963) shows that more than 95% of residues are positioned in the most favourable regions. All the residue side chains adopt standard conformations with the exception of two, Asp40 and Tyr28, the side chains of which adopt energetically slightly unfavourable χ_1–χ_2 torsion angles: the first residue, although being largely exposed to solvent, is involved in some electrostatic and hydrogen-bond interactions with water molecules, whereas for the second residue the unfavourable χ_1–χ_2 values arise from strong hydrophobic interactions and steric hindrance by neighbouring residues of the same subunit as well as by residues of the neighbouring subunit related by the twofold-symmetry molecular axis.

3.2. Structure of the subunit

The *ad* α-helix bundle is defined by the segments Thr10–Phe37, Glu45–Arg72, Thr92–Ala119 and Pro123–Val154, whereas segment Leu169–Leu177 defines the fifth *e* helix located at the C-terminal extremity (Fig. 1*a*). Helices *b* and *c* are connected by a long loop Gly74–Gly90. Helix *d* has the characteristic bending at position His132 as found in rHoLF or rBfLF. The non-helical regions are characterized by the following.

(i) At the N-terminal end, two consecutive β-turns, *i.e.* residues Ser2–Arg5 (type I) and residues Arg5–Tyr8 (type IV).

(ii) Two successive type I (residues Arg39–Val42) and type IV (residues Asp40–Ala43) β-turns at the *ab* loop and a long twisted *bc* loop (residues Gly74–Gly90) which ends with a type VIII β-turn (residues Gln86–Trp89). The main-chain orientation of residue Val81 allows its NH and CO groups to build a short antiparallel pleated sheet with the same residue of the neighbouring subunit related by a twofold axis.

(iii) At the C-terminal end, the last Leu177–Lys180 residues with well defined electron density build a type IV β-turn.

3.3. Comparison with room-temperature structure

Both protomer structures are very similar; the r.m.s. deviation of main-chain atoms is 0.15 Å. The only noticeable differences concern a few residue side chains which adopt different or alternate conformations: lowering the tempera-

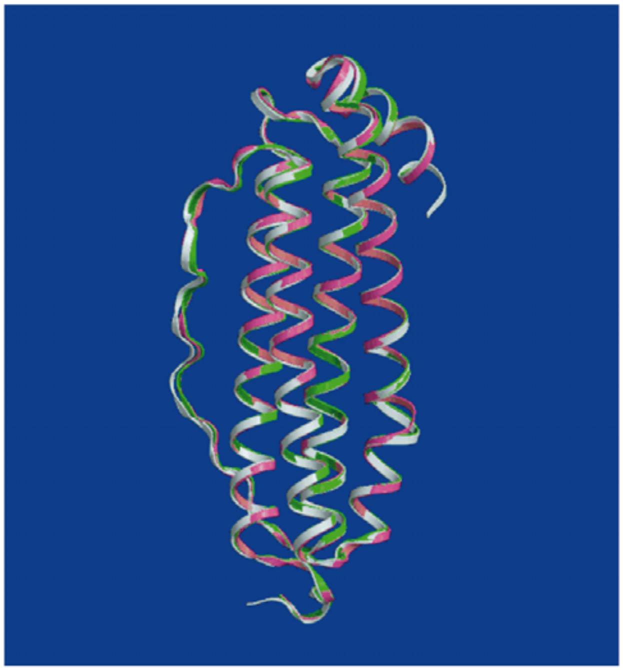

(*a*)

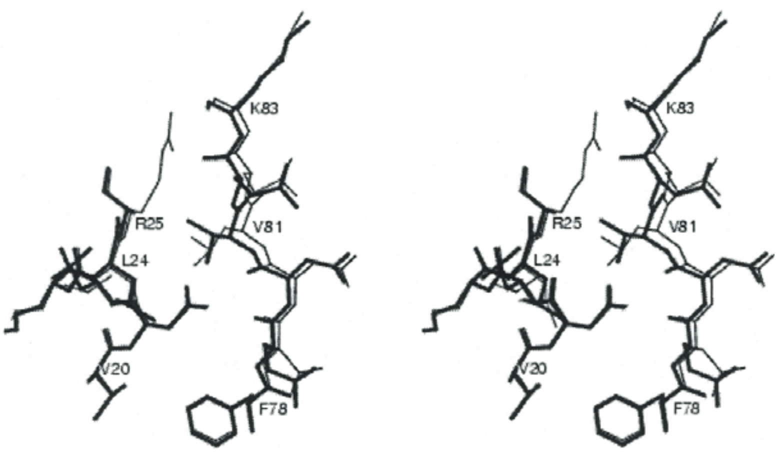

(*b*)

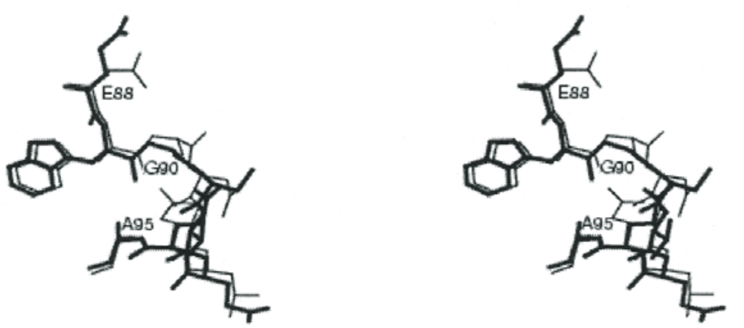

(*c*)

Figure 1
(*a*) Superposition of three subunits of rMoLF (green), rHoLF (white) and rBfLF (pink). (*b*) Stereoview of the N-terminal side of the *bc* loop fragment, for which a larger r.m.s. deviation on backbone atoms is observed between rMoLF (bold) and rHoLF (thin). (*c*) Stereoview of the C-terminal side of the *bc* loop in rMoLF (bold) and rBfLF (thin) structures.

ture allowed the positioning of six more side chains, 135 more water molecules and five more cadmium partial binding sites (see Table 2). The latter were determined, as mentioned above, with anomalous Fourier difference maps calculated with data in the range 8–2.0 Å.

3.4. Comparison with rHoLF and rBfLF

This structure exhibits a few differences from those of 1dat and 1rcd, as revealed by the C^{α} superposition of rHoLF and rBfLF onto those of rMoLF: r.m.s. deviations are 0.23 and 0.36 Å, respectively. For rHoLF, the most important differences occur in the *bc* loop and the poorly defined extremities of the *de* insertion loop of the rMoLF sequence. The deviations in the *bc* loop superposition is explained by the presence of a valine in position 81 instead of a leucine in rHoLF. The side-chain atoms of residue Val81 are embedded between the main chain of the *bc* loop and helix *a* and the bulkiness of Leu81 in rHoLF is responsible for the shift of residues 79–84 (Fig. 1*b*). For rBfLF, the greatest deviation occurs at the π-bulge position 132 in helix *d*, where a proline substitutes for a histidine in the bullfrog L-chain sequence. Differences in the backbone appear also at the end of the *bc* loop, where a type IV β-turn (Arg86–Trp89) is followed by a γ-turn (Tyr89–Asn91) (Fig. 1*c*) in the rBfLF structure.

3.5. Intrasubunit hydrogen bonds and salt bridges

Polar and electrostatic interactions are listed in Table 3 and are compared with those of rHoLF, to which they are very similar (70% interactions conserved). A major difference with this latter concerns the salt bridge embedded within the four-helix bundle: this salt bridge is a common feature of L-chain ferritins and substitutes the ferroxidase centre observed in H-chain ferritins. In the present structure, several differences from the horse L-chain sequence, *i.e.* Leu102Met, Phe133Tyr, Glu136Lys and particularly Tyr23His substitutions, noticeably modify the environment of the conserved Lys58–Glu103 electrostatic interaction: the Tyr23His substitution leads to the presence of a water molecule which binds His23 N^{ε} and occupies the space held by Tyr23 OH in rHoLF: Fig. 2 depicts the penetration of water molecules inside the four-helix bundle. In rBfLF, an electrostatic interaction is observed between Lys23 and Glu58. These three examples show that a strong variability is allowed for this salt bridge, which has been mentioned as playing an important role in the thermal stability of L-chain ferritins (Hempstead *et al.*, 1997; Martsev *et al.*, 1998).

3.6. Hydrophilic interactions upon shell assembly

Among the polar and salt-bridge interactions listed in Table 3, 24 involve residues from neighbouring subunits. Interactions with solvent water molecules are depicted in more detail in the present structure, where 286 water molecules have been located, of which 192 belong to the first shell. Among these latter water molecules, 47 connect neighbouring subunits and are shown in Fig. 3 along with the intersubunit electrostatic and polar interactions. Fig. 3 underlines the small number of non-water interactions present in the vicinity of the threefold axes, the entry route of iron ions into the ferritin shell.

3.7. Hydrophobic interactions upon shell assembly

The ferritin subunit exhibits on its external surface noticeable hydrophobic regions which are buried upon assembly of the protein shell. Two of these regions were previously depicted in the structures of rHoLF (Ford *et al.*, 1984) and of rHuHF (Lawson *et al.*, 1991; Hempstead *et al.*, 1997). An attempt to describe these hydrophobic surfaces is carried out using the software *QUILT* (Lijnzaad *et al.*, 1996; Lijnzaad & Argos, 1997). The surface values of the six largest hydrophobic patches are listed in Table 4, along with those of their fractions which remain exposed to the solvent after the shell assembly. Patches 1 and 2 display large values (about 600 $Å^2$ each) and correspond to the interface regions generated by the twofold and fourfold symmetry axes: they are 80% buried when the protein shell is assembled. Less extended patches 3 and 4 are also 50 and 80% buried upon shell assembly. Fig. 4 shows the various proportions of accessible areas of one subunit, as well as their fractions buried upon shell assembly. It allows us to note the following. When subunits assemble, the proportion of buried hydrophobic and hydrophilic areas remains constant at about 60 and 40%, respectively. However, the contribution of the four largest hydrophobic patches to the buried hydrophobic area is predominant: whilst they represent 31% of the accessible hydrophobic area (Fig. 4, column 1), their buried fraction upon shell assembly represents 56% of the hydrophobic buried area (Fig. 4, column 2). On the other hand, small hydrophobic patches, the areas of which are less than ~200 $Å^2$, do not seem to contribute to shell assembly: the first water shell shields most of these patches as well as polar residues (Fig. 4, column 3). For example, patch number 6, listed in Table 4, is almost masked by ordered water molecules which bind neighbouring polar residues.

Therefore, the four largest hydrophobic patches listed in Table 4 definitely play an active role during shell assembly of the ferritin molecule.

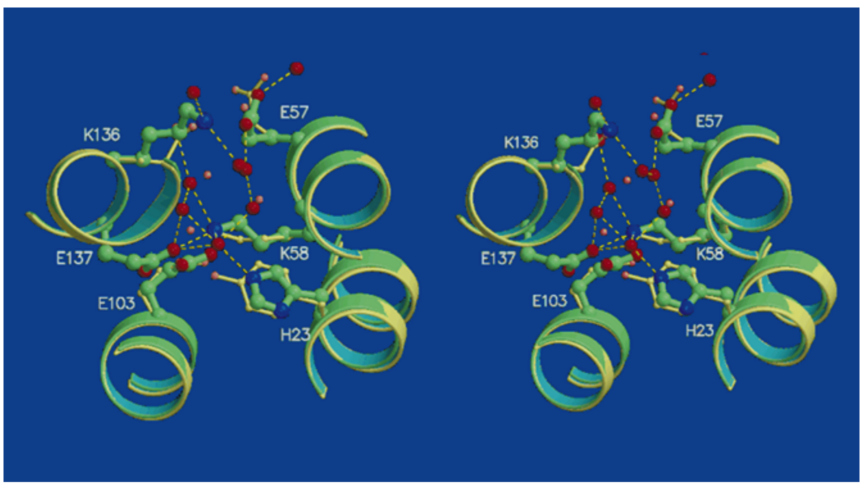

Figure 2
The salt bridge embedded within the four α-helix bundle of rMoLF (thick green bonds and ribbons, large-radius atoms) and rHoLF (thin yellow bonds and ribbons, small-radius atoms). Hydrogen bonds and electrostatic interactions are shown for the rMoLF structure only.

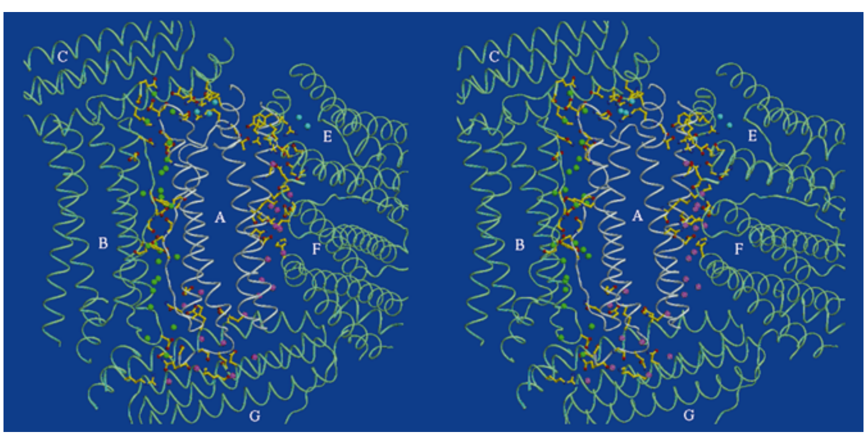

Figure 3
Stereoview of shell assembly. Subunit *A* is related to neighbours by 432 symmetry, subunit *B* by twofold symmetry, subunits *C* and *E* by fourfold symmetry, and subunit *F* and *G* by threefold symmetry. Main- and side-chain atoms of residues involved in intersubunit hydrogen bonds and salt-bridge interactions are shown, along with water molecules which bind atoms of two or more different subunits.

3.8. Metal-binding sites

Cadmium-binding sites were determined from anomalous Fourier difference maps. Residues involved in cadmium-binding sites are listed in Table 5. They are identical to those previously found in rHoLF (Granier *et al.*, 1998 and references therein): Asp80 and Gln82 for intermolecular contacts; Glu53, Glu56, Glu57 and Glu60 for the ferrihydrite nucleation centre; and His114, Glu130, Asp127 and His132 for the threefold-axis entry route of iron ions. Only one exception, an additional site, is found at His49, close to the nucleation centre. Average distances are 2.19 and 2.27 Å for Cd—O and Cd—N^{δ} (histidine) bonds, respectively. As regards the coordination of the various sites, only those of Asp80, Gln82 (square planar) and His132 (octahedral) are well defined, whereas those located on the threefold axis (His114, Glu130 and Asp127)

Table 4
Hydrophobic patches at the subunit external surface.

See Fig. 3 for labels for intersubunit contacts. Values are in Å^2.

Patch No.	Residues involved	Symmetry involved	Accessible area for a single subunit	Remaining accessible area per subunit after shell assembly	After shell assembly including solvent
1	Tyr28, Phe35, Arg59, Glu63, Phe78, Gln79, Val81	Twofold axis *A–B*	603	100	51
2	Arg153, Ser168, Leu169, Tyr172, Leu173, Arg176	Fourfold axis *A–C*	591	116	59
3	Leu100, Ala101, Met102, Lys104, Ile141, Lys142, Gly145, Leu148	Threefold axis *A–F*	230	119	2
4	Leu111, His114, Glu130, Leu134	Threefold axis *A–G*	217	44	0
5	Leu22, Arg25, Gln82, Asn105, Ala109	Outer-shell side	175	175	45
6	Phe50, Leu54, Glu57, Lys136, Leu140, Lys143	Inner-shell side	176	176	7
Total			1992	730	164

Table 5
Residues involved in cadmium-binding sites.

Side-chain density correlation coefficients and average shifts (Å) are from *SFCHECK*.

	300 K		100 K	
Residue	D_{corr}	Shift (Å)	D_{corr}	Shift (Å)
His49	0.95	0.17	0.96	0.13
Glu53	—	—	0.90	0.13
Glu56	—	—	0.96	0.09
Glu57	0.91	0.16	0.95	0.10
Asp80	1.0	0.04	1.0	0.06
Gln82	0.98	0.10	0.94	0.09
Glu60	0.89	0.19	0.98	0.05
His114	1.0	0.06	0.99	0.02
Cys126	1.0	0.04	0.97	0.03
Asp127	1.0	0.04	1.0	0.07
Glu130	0.98	0.09	1.0	0.07
His132	0.99	0.07	1.0	0.03

as well as those at the nucleation site (His49, Glu53, Glu56, Glu57, Glu60) are incompletely determined owing to threefold symmetry disorder, statistical disorder or incomplete determination of coordinated water molecules.

4. Conclusions

The structure of rMoLF has been determined at 1.6 Å resolution under cryogenic conditions. The protomer shows little differences from two other L-chain ferritin structures, *i.e.* those of horse and bullfrog. The structure of the eight-amino-acid insertion PAQTGAPQ, located in the *de* loop could not be determined at either room temperature or at low temperature. This part of the structure is strongly disordered as previously observed in the room-temperature structure of the recombinant rat L-chain ferritin (Lawson, 1990). The major difference from rHoLF and rBfLF concerns the salt bridge embedded within the four-helix bundle of the subunit. In rMoLF, the presence of a histidine in position 23 instead of a tyrosine or a lysine is compensated by the penetration of water molecules into the helix bundle.

The hydrogen bonds and salt bridges are highly conserved: 24 of them participate in the shell assembly along with 47 water molecules. All interface regions are involved with the exception of the vicinity of the threefold-axis interface (the iron-entry route).

The metal-binding sites are identical to those observed in rHoLF, with the exception of a new site involving a histidine in position 49. This residue is highly conserved in mammalian L-chain ferritins and could be considered as part of the ferrihydrite nucleation centre.

Six large hydrophobic patches located at the subunit external surface have been described using the procedures of Lijnzaad *et al.* (1996). Four of them seem to actively participate in the assembly process of the ferritin subunits into the protein shell. The two largest patches correspond to interface

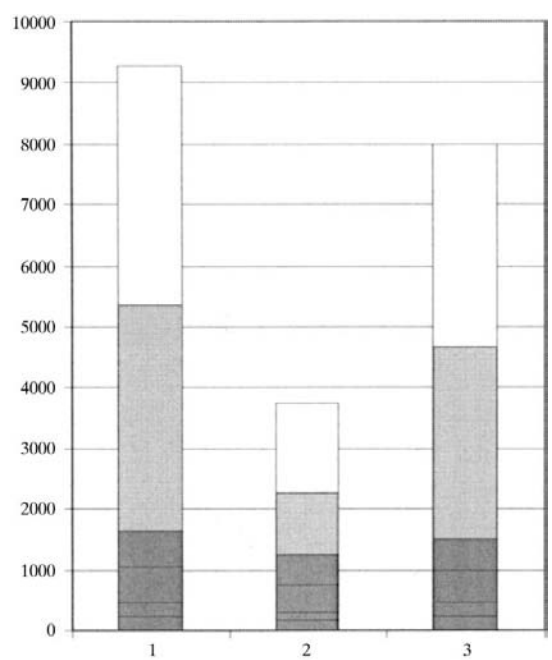

Figure 4
Variation of the hydrophilic (white) and hydrophobic (grey) surfaces (Å^2) of a rMoLF subunit: accessible surface of a subunit (column 1), buried surface upon shell assembly (column 2) and non-accessible surface upon shell assembly, taking into account ordered water molecules of the first hydration shell (column 3). The contribution of the four largest hydrophobic patches is shaded in dark grey.

regions of subunits related by twofold and fourfold symmetries, whereas the third and fourth patches involve subunits related by threefold symmetry.

We are grateful to Professor D. Moras, Dr Mitschler and A. Litt from the Laboratoire de Biologie Structurale (Institut de Génétique et de Biologie Moléculaire et Cellulaire), Strasbourg for providing us with the design of their modified Huber goniometer head equipped with a removable arc.

References

Adelman, T. G., Arosio, P. & Drysdale, J. W. (1975). *Biochem. Biophys. Res. Commun.* **63**, 1065–1062.

Beaumont, C., Dugast, I., Renaudie, F., Souroujon, M. & Grandchamp, B. (1989). *J. Biol. Chem.* **264**, 7498–7504.

Chasteen, N. D. & Harrison, P. M. (1999). *J. Struct. Biol.* **126**, 182–194.

Clegg, G. A., Stanfield, R. F. D., Bourne, P. E. & Harrison, P. M. (1980). *Nature (London)*, **288**, 298–300.

Collaborative Computational Project, Number 4 (1994). *Acta Cryst.* D**50**, 760–763.

Cruickshank, D. W. (1999). *Acta Cryst.* D**55**, 583–601.

Diederichs, K. & Karplus, P. A. (1997). *Nature Struct. Biol.* **4**, 269–275.

Ford, G. C., Harrison, P. M., Rice, D. W., Smith, J. M. A., Treffry, A., White, J. L. & Yariv, J. (1984). *Philos. Trans. R. Soc. London Ser. B*, **304**, 551–565.

Granier, T., Comberton, C., Gallois, B., Langlois d'Estaintot, B., Dautant, A., Crichton, R. R. & Précigoux, G. (1998). *Proteins*, **31**, 477–485.

Granier, T., Gallois, B., Langlois d'Estaintot, B., Dautant, A., Comberton, G., Mellado, J. M., Beaumont, C., Santambrogio, P., Arosio, P. & Précigoux, G. (2000). *Acta Cryst.* D**56**, 634–636.

Gallois, B., Langlois d'Estaintot, B., Michaux, M.-A., Dautant, A., Granier, T., Précigoux, G., Soruco, J.-A., Roland, F., Chavas-Alba, O., Herbas, A. & Crichton, R. R. (1997). *J. Biol. Inorg. Chem.* **2**, 360–367.

Harrison, P. M. & Arosio, P. (1996). *Biochim. Biophys. Acta*, **1275**, 161–203.

Harrison, P. M., Hempstead, P. D., Artymiuk, P. J. & Andrews, S. C. (1998). *Met. Ions Biol. Syst.* **35**, 435–477.

Hempstead, P. D., Yewdall, S. J., Fernie, A. R., Lawson, D. M., Artymiuk, P. J., Rice, D. W., Ford, G. C. & Harrison, P. M. (1997). *J. Mol. Biol.* **268**, 424–448.

Lawson, D. M. (1990). PhD thesis, University of Sheffield, England.

Lawson, D. M., Artymiuk, P. J., Yewdall, S. J., Smith, J. M., Livingstone, J. C., Treffry, A., Luzzago, A., Levi, S., Arosio, P., Cesareni, G., Thomas, C. D., Shaw, W. V. & Harrison, P. M. (1991). *Nature (London)*, **349**, 541–544.

Leslie, A. G., Brick, P. & Wonacott, A. J. (1986). *CCP4 Newsl.* **18**, 33–39.

Lijnzaad, P. & Argos, P. (1997). *Proteins*, **3**, 333–343.

Lijnzaad, P., Berendsen, H. J. & Argos, P. (1996). *Proteins*, **2**, 192–203.

Litt, A., Arnez, J. G., Klaholz, B. P., Mitschler, A. & Moras, D. (1998). *J. Appl. Cryst.* **31**, 638–640.

McRee, D. E. (1993). *Practical Protein Crystallography*. New York: Academic Press.

Martsev, S. P., Vlasov, A. P. & Arosio, P. (1998). *Protein Eng.* **11**, 377–381.

Murshudov, G. N., Vagin, A. A. & Dodson, E. J. (1997). *Acta Cryst.* D**53**, 240–255.

Ramachandran, G. N., Ramakrishnan, C. & Sasisekharan, V. (1963). *J. Mol. Biol.* **7**, 95–99.

Roussel, A., Fontecilla-Camps, J. C. & Cambillau, C. (1990). *Acta Cryst.* A**46**, C66–C67.

Santambrogio, P., Cozzi, A., Levi, S., Rovira, E., Magni, F., Albertini, A. & Arosio, P. (2000). *Protein Expr. Purif.* **19**, 212–218.

Takagi, H., Shi, D., Ha, Y., Allewell, N. M. & Theil, E. C. (1998). *J. Biol. Chem.* **273**, 18685–18688.

Trikha, J., Theil, E. C. & Allewell, N. M. (1995). *J. Mol. Biol.* **248**, 949–967.

Vaguine, A. A., Richelle, J. & Wodak, S. J. (1999). *Acta Cryst.* D**55**, 191–205.